Journal of Micromechanics and Microengineering

PAPER

Key kinematic parameters in a low-loss power splitter written by femtosecond laser micromachining

IOP Publishing Journal of Micromechanics and Microengineering

J. Micromech. Microeng. **28** (2018) 055011 (8pp) https://doi.org/10.1088/1361-6439/aaafe8

Key kinematic parameters in a low-loss power splitter written by femtosecond laser micromachining

R Peyton[1,2], V Guarepi[1], F Videla[1,3] and G A Torchia[1,2]

[1] Centro de Investigaciones Ópticas (CONICET-CICBA-UNLP), M.B. Gonnet (1897), Buenos Aires, Argentina
[2] Departamento de Ciencia y Tecnología, Universidad Nacional de Quilmes, Bernal (1876), Argentina
[3] Facultad de Ingeniería, Universidad Nacional de la Plata, Depto de Ciencias Básicas, La Plata (1900), Argentina

E-mail: robertop@ciop.unlp.edu.ar (R Peyton) and gustavot@ciop.unlp.edu.ar (G A Torchia)

Received 28 November 2017, revised 12 February 2018
Accepted for publication 16 February 2018
Published 13 March 2018

Abstract

In this work we design, fabricate and characterize a 1 × 2 Y-branch power splitter based on simplified coherent coupling. This device was constructed by type II waveguide structures inscribed by a direct femtosecond laser writing technique in x-cut lithium niobate crystal. First of all, a theoretical study that links the kinematic and writing fluence of the process is developed, which allows us to establish the design trade-off and justify the best geometry chosen. Then, the design was optimized and tested by using commercial software, resulting in a compact and low-loss photonic circuit. The efficiency of the proposed device is compared with two others: a curved and a straight splitter. Finally, the experimental results were compared with simulations and then a statistical analysis of multiple comparisons was also conducted, obtaining 3.7 dB ± 0.1 dB insertion losses and 4.5% of the unbalanced coupling ratio.

Keywords: femtosecond laser writing, lithium niobate, coherent coupling

(Some figures may appear in colour only in the online journal)

1. Introduction

Currently, photonic devices are used in many applications. In particular, we would like to stress the great importance they have in optical and quantum communications, among other applications [1–3]. There are different manufacturing techniques [4, 5]; however, direct writing with femtosecond micromachining has some attributes that stand out from the rest. In this sense, the main advantages of the method are: the practicality of building three-dimensional devices, the rapidity with which prototypes are obtained and the variety of materials that can be used [6, 7]. The direct writing of waveguides lies in a localized modification of the refractive index of a dielectric. This is achieved by focusing a femtosecond laser pulse with sufficient energy below the sample surface. The optical waveguides fabricated with femtosecond laser micromachining are classified according to refractive index changes induced in the irradiated regions. The best known are Type I (the index increased in the irradiated region) and Type II (index decreased near the exposed region). In this work, type II waveguides are used because they have a better performance—as the light-guided area usually preserves the material properties—and, above all, are more stable from the thermal point of view. Usually, these configurations are two parallel tracks with a suitable separation and the structure 'double-line' forms the limits of the nucleus where the light is confined. This tight modification, combined with a translation of the material, makes it possible to manufacture waveguides with complex geometries, by using a motorized movement station controlled by a computer. From a kinematic perspective, the quality of the inscribed waveguides depends on the mechanical precision and uncertainties associated with the control of the micromachining station.

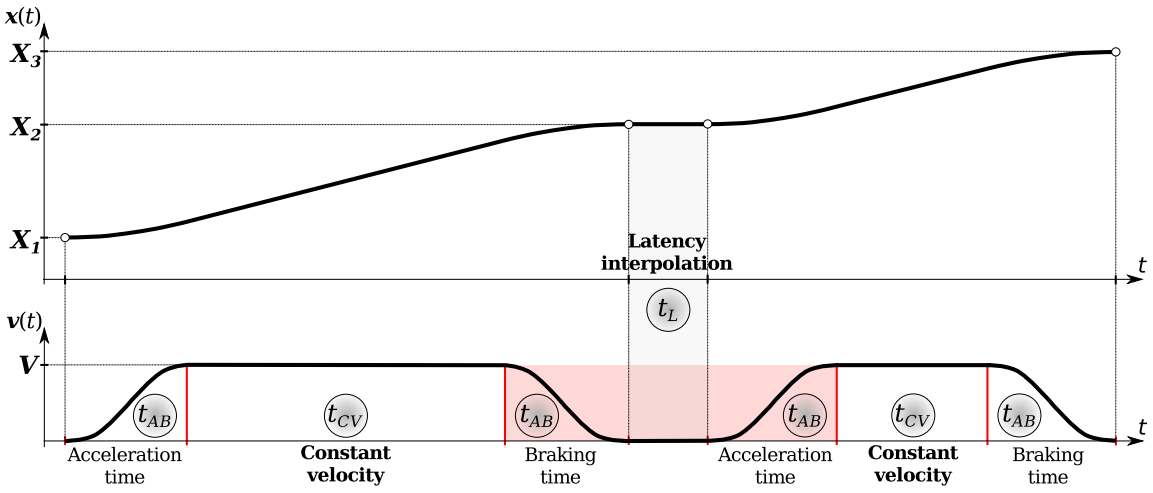

Figure 1. Kinematic profile of a motorized motion station.

Although there is not yet a physical model that fully describes this process, many authors have already reported the influence of each of the process parameters (pulse duration, energy, focus characteristics, repetition frequency and velocity) on waveguides' characteristics in different materials [7, 8]. The width and energy of the pulse are parameters that determine the morphology of the interaction; they depend heavily on the material and type of waveguide. The focus influences the size and geometry of the writing spot and also relates to the distance from the surface and the type of microscope objective. The pulse repetition frequency and scan velocity are parameters of great incidence in writing quality. This is linked especially to the nonlinear absorption regime, thermal transfer to lattice, and process energy relaxation [9].

From another perspective, movement dynamics depends on the type of motor driver. In general, there are different types of micromachining stations. Today, the equipment uses a speed profile achieving soft, rapid and precise movements. However, the trajectories depend on the motor driver model: the most cheap and ordinary allow synchronized movements point to point; while the more advanced system can follow a path that may not be linear or differentiable [10, 11]. Movements that transit through several points are known as interpolation. It is a parameter that could significantly influence writing process dynamics [12–14]. For this reason, it is important to associate the limitations of the motorized movement station with optical losses for the devices.

In this work we design and characterize a 1×2 Y-branch power splitter in x-cut LiNbO3 with a femtosecond direct writing technique. After an analysis of the kinematic and fluency of the process, a geometry with simplified coherently coupled multi-sectional bends is fabricated [15]. The performance of this device is compared with two other typical splitters (curved and straight). A comparison of the simulated and experimental results is presented.

2. Materials and procedures

In this paper, we study three power splitters fabricated with a direct writing technique in x-cut LiNbO3 crystals, based on type II waveguides written by a chirped pulse amplification system (CPA) at 800 nm on a Ti:sapphire ultrafast laser. The pulse duration is 150 fs with 1kHz repetition rate and a pulse energy of 0.7 μJ. A 20 $\times$ (N.A. $= 0.4$) microscope objective is used to focus the laser at 200 μm below the crystal surface. A Newport micrometer motorized station system with an accuracy of about $\pm$275 nm is used. The station is composed of three SMC100CC controllers for the three servo motors, two horizontal UTS50CC and one vertical UZS80CC. The trajectory is constructed from a development application that allows one to execute three-dimensional geometries previously programmed in files with the coordinates to interpolate. This micromachining station only allows synchronized movements with an S-gamma velocity kinematic profile (see the details in figure 1) [16]. Interpolation latency is the minimum time that the system takes from one end point to the next, and this value is between 50 to 100 ms.

Numerical simulations are performed using the beam propagation method (BPM), which uses paraxial approximations of the Helmholtz equation assuming that the envelope amplitude of the electromagnetic field varies smoothly in the direction of propagation. For this, a commercial RSoft calculation software is used, in particular the BeamProp tool, which uses the finite element method of Crank–Nicholson [1, 17]. In the simulations we have used a refractive index profile previously reported, this describes the morphology of the type II waveguides inscribed in LiNbO3 [18].

The direct light coupling technique or 'end-fire' method is used for the measurements of optics performed by the splitters. The spatial intensity distribution of the modes is measured with a Newport LBP2 beam analyzer by placing a microscope objective at the output of the device. The light source used in the experiment was a 980 nm laser diode with 20 mW optical power.

3. Theoretical framework

3.1. Kinematic analysis

The motorized movement station uncertainties and limitations can affect the quality of the fabricated device, so before

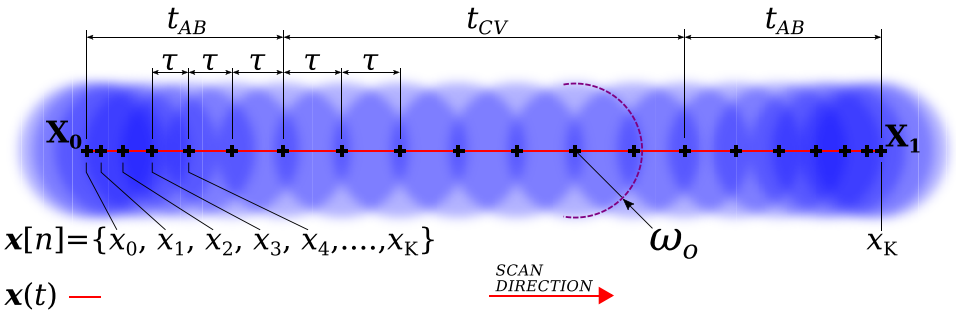

Figure 2. Schematic of displacement and discretization incident pulses for each τ period.

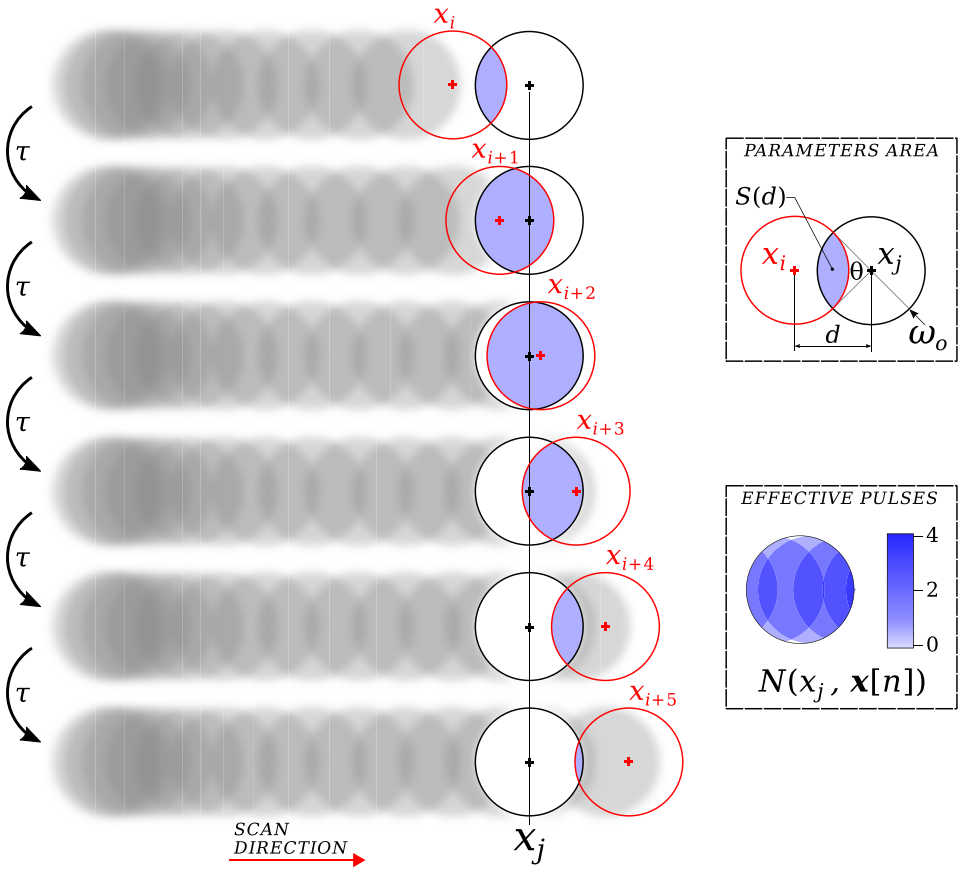

Figure 3. Temporal scheme of incident pulses. Each τ period is evaluated at $\mathbf{x_j}$. In the southeast sector we show the 'effective pulses number per spot'. In the northeast sector we show how the intersection area is calculated.

designing an optical circuit, certain characteristics of the motor driver must be known. In general terms, there are three parameters to take into account: uncertainty in position, movement types allowed and kinematic profile. Figure 1 shows the kinematic response of the system to an interpolation between $\mathbf{X_1}$, $\mathbf{X_2}$ and $\mathbf{X_3}$ points. Function $\mathbf{x}(t)$ and $\mathbf{v}(t)$ are temporal variations of position and velocity, respectively. The configuration parameters are determined by spatial coordinate $\mathbf{X}$ speed $\mathbf{V}$ acceleration $\mathbf{A}$ and jerk time $\mathbf{t_j}$. As shown in figure 1, three time intervals are defined according to velocity behavior: t_{AB} is the time interval where the velocity derivative is non-zero, that is, when the system is accelerating or breaking; t_{CV} system moves at constant speed; and t_{L} is the interpolation latency time.

These process parameters must be constant in order to achieve a good quality in writing, i.e. the pulse duration and energy, focus characteristic, repetition rate and scan velocity should be the same at all times [9]. Analyzing this, it can be observed that the motor driver used in this work imposes a dynamic limitation on displacement because the micromachining station does not allow us to interpolate at constant speed. The acceleration and braking time can be minimized by increasing the acceleration constant, however, the maximum value is limited by the jerk time ($\mathbf{t_j}$, a parameter that is left fixed according to the manufacturer's recommended configuration so as not to damage the mechanical system) and the speed configuration parameter. In this way, the best kinematic configuration of the micro-machining station is $\mathbf{A} = \mathbf{V}/\mathbf{t_j}$,

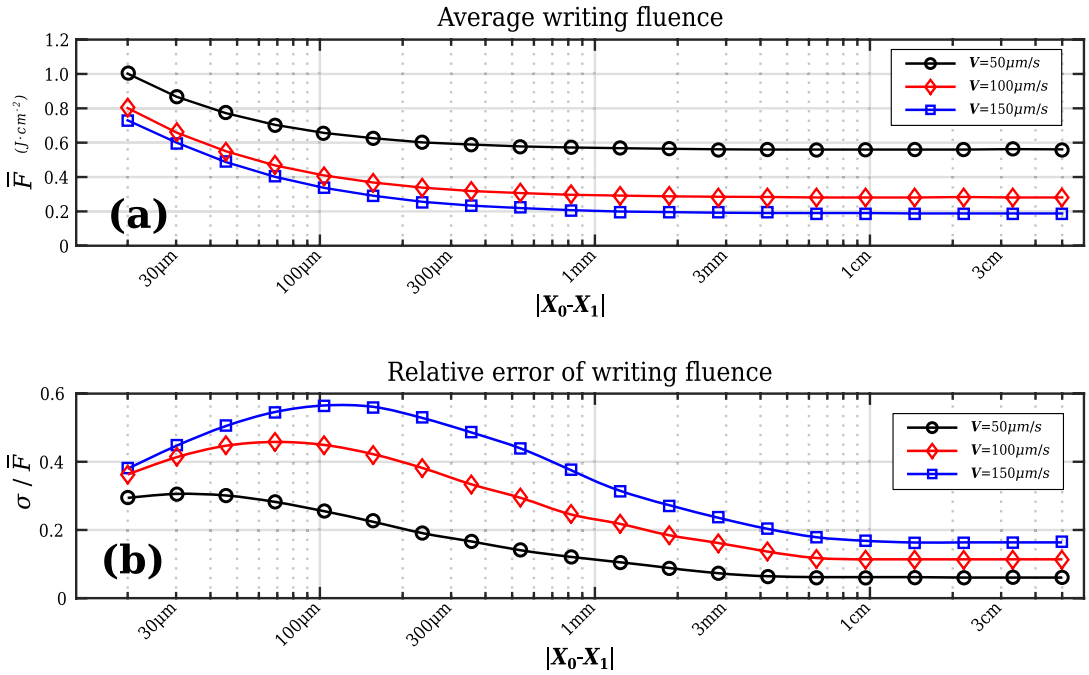

Figure 4. Simulated energy dynamics of the process for different displacement and velocity range. (a) Average writing fluence, (b) relative error writing fluence.

where the only variable to be configured is the velocity **V**. In this sense, there is a trade-off between the amount of interpolation points and the scan velocity. To further examine this aspect, the relationship between the displacement kinematic and energy deposited by the surface unit (writing fluence) is analyzed below.

3.2. Fluence analysis

From the kinematic point of view, the direct writing technique is based on the combination of a spatial displacement and pulses emitted at each period $\tau = 1/f$, where f is the repetition rate, obtaining an incident pulse sequence separated by a distance that will depend on the kinematic. Since pulse temporal width is extremely small compared with displacement, each pulse can be represented as a spot in the trajectories space. In this sense, figure 2 shows a scheme that describes this behavior between $\mathbf{X_0}$ to $\mathbf{X_1}$. As can be seen, the pulses in the t_{CV} interval are equidistant while t_{AB} follows a cubic relationship, since the acceleration has a trapezoidal profile [10, 11]. The coordinates of each pulse are obtained from the discretization of $\mathbf{x}(t)$ in $\mathbf{x}[n]$:

$$\mathbf{x}[n] = \mathbf{x}(k\tau), \forall k \in \mathbb{N} : k = \{0, 1, 2, 3, ..., \mathrm{K}\}. \quad (1)$$

However, neglecting the lens aberrations and nonlinear propagation effects in the dielectric, the spot has an area that depends on the focus characteristics. The intensities spatial profile can be approximated by a paraxial equation wave and Gaussian optics. The spot is located at the focus of the lens, with ω_o radius being minimal and limited by diffraction, known as the Gaussian beam waist [1]. Although it is known that the beam has an intensities Gaussian spatial distribution, for the practical purposes of this study it is valid to assume a constant distribution of energy E, since we want to describe the behavior of fluence in a macroscopic way. Alternatively, it is possible to consider a spatially filtered region of the Gaussian beam where the intensity distribution can be considered to be almost constant.

At low frequency rates (<100 kHz) the changes generated by each pulse are independent of the following pulse, so that the thermal diffusion effects are negligible and therefore the waveguide is formed by the pulses' superposition in one spot (see figure 3) [9]. As the separation between two adjacent pulses depends on speed, it is observed that each interpolation point of the motorized motion station imposes a variation in superposition pulse rates. To quantify this behavior a factor called the *'effective pulses number per spot'* is used:

$$N(\mathbf{x_j}, \mathbf{x}[n]) = \sum_{i=0}^{K} \frac{S(|\mathbf{x_j} - \mathbf{x}[n]|)}{\pi\omega_o^2} \quad (2)$$

where $\mathbf{x_j}$ is a trajectory coordinate to evaluate and $S(|\mathbf{x_j} - \mathbf{x}[n]|)$ is an intersection area of two disks of the radius ω_o located at a distance $|\mathbf{x_j} - \mathbf{x}[n]|$:

$$S(d) = \omega_o^2 \left[\theta(d) - \sin\left(\theta(d)\right)\right] \quad (3)$$

where $\theta(d)$ is the angle formed between the intersection points of two circumferences and the distance d between centers:

$$\theta(d) = 2 \arccos\left(\frac{|d|}{2\omega_o}\right), \forall d \in \mathbb{R} : |d| < 2\omega_o. \quad (4)$$

Figure 3 shows a diagram of equation (2) for different times and equation (1) for different positions. Furthermore,

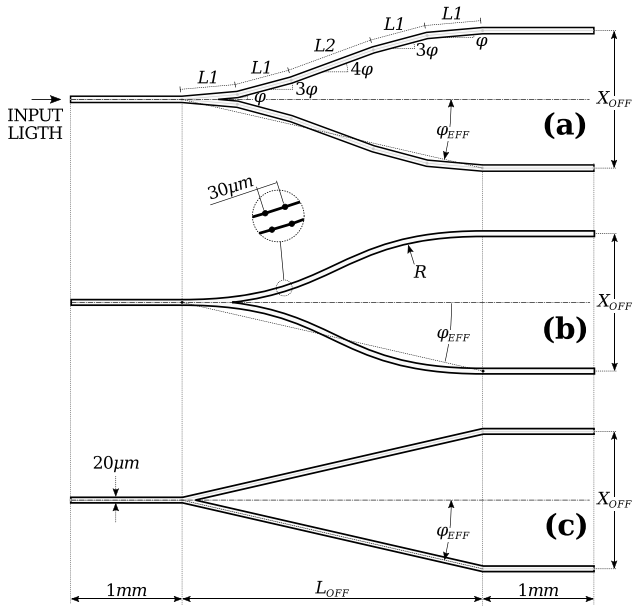

Figure 5. Dimensions of power splitters used. (a) CCS splitter, (b) curved splitter, (c) straight splitter.

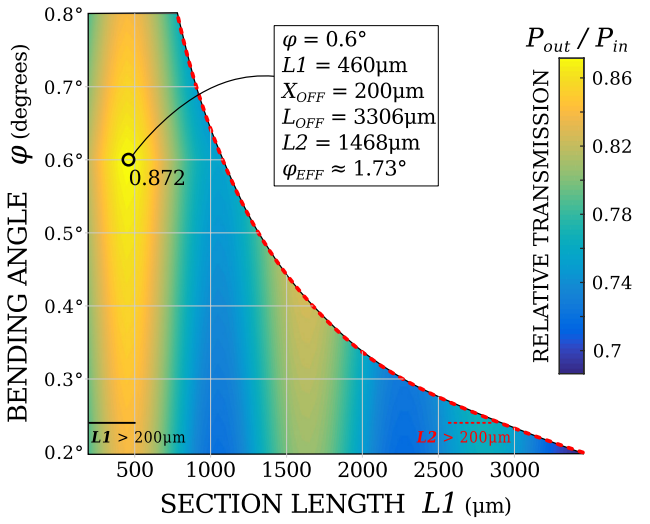

Figure 6. CCS splitter loss calculation. The text-box shows the dimensions where losses are minimized. $\Omega : \{\{0.2° < \varphi < 0.8°\} \cap \{L1 > 200\ \mu\text{m}\} \cap \{L2 > 200\mu\text{m}\}\}$.

on the right side, using parameters to calculate, the intersection area of equations (3) and (4) are displayed.

The writing fluence is defined as the energy radiated in space trajectories per spot area, expressed in J· cm^{-2}:

$$F(\mathbf{x_j}) = \frac{\mathrm{E}}{\pi\omega_o^2} N(\mathbf{x_j}, \mathbf{x}[n]) \tag{5}$$

where $\mathrm{E}/\pi\omega_o^2$ is the fluence of one pulse. Equation (5) shows that $F(\mathbf{x_j})$ is proportional to the '*effective pulses number per spot*', and therefore writing fluence is a parameter that depends directly on the kinematics of the writing process.

In addition, figure 4(a) show the average of writing fluence ($\bar{F}$) between $\mathbf{X_0}$ and $\mathbf{X_1}$, where 30 μm $< |\mathbf{X_0} - \mathbf{X_1}| <$ 5 cm for three different speeds (50, 100 and 150 μm · s^{-1}), and for jerk time 0.04 s. The acceleration is 1250, 2500 and 3750 μm · s^{-2}, respectively. The writing parameters are: pulse energy (0.7 μJ), spot waist (1.6 μm) and period (1 ms). This plot shows that $\bar{F}$ is inversely proportional to $|\mathbf{X_0} - \mathbf{X_1}|$ and for $|\mathbf{V}|$. Also, figure 4(b) shows the relative error of the writing fluence ($\sigma/\bar{F}$); this decreases with distance and increases with scan velocity.

In conclusion, to minimize error or variability of the writing fluence it is necessary to increase the distance between the interpolation points. How does this condition affect the design of optical devices? Let us look at an example. A Y-branch power splitter is common to use with curved geometries, which may be based on sinusoidal, polynomial or circular curves. It can seen above that these paths could only be approximated by small adjacent straight sections with the motorized movement station used in this work. Therefore, shorter distances will be a better curve approach, i.e. minor error in approximation. So this is where we find a design trade-off: reduce the approximation error by increasing the amount of interpolation points; or decrease the error in the writing fluence by increasing the distance of the straight sections. In the next section, a design that reduces the amount of interpolation points using simplified coherent coupling (CCS) is proposed [15].

3.3. Simplified coherent coupling

Coherent coupling is a technique to bend light through small straight waveguides with sharp bending. Several studies have already reported deviators and splitters with low-loss, compact and efficient devices, compared with other types of geometries. In 1974, Taylor [19] showed that curvature loss is an oscillatory function that depends strongly on section length L, due to the coupling between guided and radiated modes. Physically, light decoupled in a curve can be coupled back into a subsequent curve if the difference between the modes' phase (guided and unguided) is an odd multiple of π. Throughout the 1980s, Jhonson *et al* [20] showed that optimizing L greatly reduces curved losses. In 2002, Su and Wang [21] presented simplified coherent coupling, developed to be even more compact with smaller geometries and smaller losses than their predecessors. Innovation was sought to eliminate the phase variation of the wavefront at each curvature by changing the angle between each section. From these results, in 2003, Hsu *et al* [15] proposed a compact Y-branch power splitter based on simplified coherent coupling, compact and insensitive to variations in the wavelength. So, in this paper we will base our design on reducing the amount of interpolation points and thus reducing the uncertainty of the writing fluence, being in consequence, more compact and efficient than those designed with radial, sinusoidal or polynomial bends.

In figure 5(a) a schematic diagram of a (modification of a design by Hsu) splitter (CCS) is proposed. This consists of a straight waveguide input of 1 mm, a branching structure and two straight waveguide output of 1 mm. The deviation of each branch is symmetrical and conducted through a sequence of five straight segments with angles φ, 3φ, 4φ, 3φ and φ, as shown in figure 5(a). Varying $L1$ and φ optimizes the geometry,

separation between outputs is fixed at $X_{\mathrm{OFF}} = 200\ \mu$m and hence the length $L2$ remains as a function of these parameters.

To characterize device performance, it is compared to two types of power splitters that have the same bend angle, but using another geometry. The first is the curved splitter of figure 5(b), this is a circuit where light deviation is achieved from two tangent arcs linking inputs and outputs with straight waveguides. The curves are divided into small straight segments of 30 μm that an increasing relative error in writing fluence. The second is a straight splitter, the input and output are connected by a straight waveguide with an angle equal to effective angle φ_{EFF}, as shown in figure 5(c). Here the distance between interpolation points is maximized, which reduce relative error in the writing fluence. As a result, it is analyzed with three optical power splitter, each with a different quality: the curved splitter reduce approximation error by increasing amount of interpolation points, the straight splitter decrease error in writing fluence increasing distance of straight sections, and the CCS splitter is a hybrid of both. Note that, in the three designs, the connection with the straight waveguide input and the branches are no-offset type, since them allows better compare the differences of coupling ratio and light division between designs.

4. Results and discussions

The total relative transmitted power of the CCS splitter is calculated with RSoft simulation software. The angle φ is varied from 0.2° to 0.8° and the lengths of the $L1$ and $L2$ sections are greater than 200 μm. Figure 6 shows the simulation result. The oscillatory behavior of the losses ($P_{\mathrm{out}}/P_{\mathrm{in}}$) as a function of $L1$ is shown in figure 6 as the model predicts.

The efficiency is optimized with $L1 = 460\mu$m and $\phi = 0.6°$. Under this configuration the $L2$ section is 1468 μm and the general dimensions of the device X_{OFF}, L_{OFF} and φ_{EFF} are 200 μm, 3306 μm and 1.73°, respectively. It can be seen that the central section $L2$ is much larger than $L1$, thus ensuring symmetry of the coherent coupling between input-output [15]. The device is compact because the losses and L_{OFF} length are minimized in the northeastern section of the presented plot.

The simulation results are shown in figure 7. The curved splitter (dotted line) of figure 5(b) has a curvature radius $R = 27.3$ mm, verifying the condition of low loss reported for these geometries [22]. However, curvature losses are predominant in the straight splitter (dashed line) [23].

The graph of figure 7 shows the difference between the propagation (in the shadowed region) and curvature losses of the devices. Differences are observed between the losses slopes and where they are occurring: the CCS splitter has a behavior similar to the straight waveguide; the curved splitter is separated from those in the outlet section; and the straight splitter has large losses due to the bending angle, since decoupled light at the beginning does not couple again. Moreover the negative slope of the straight guide after 3.5 mm of a propagation loss constant of 1.44 dB · cm^{-1} is observed.

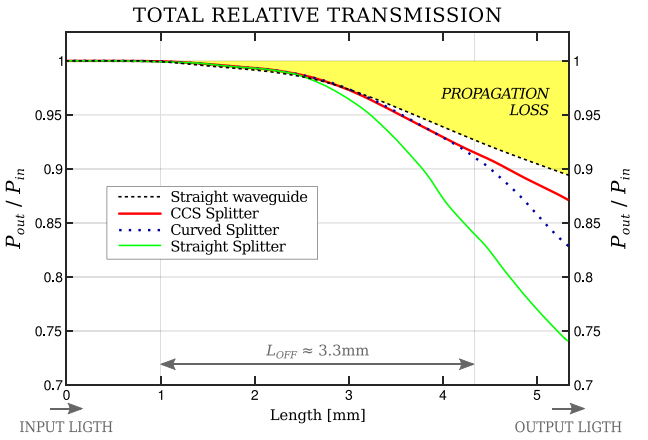

Figure 7. Total relative transmission along the propagation direction in the power splitter takes into account the sum of both branches. In the shadowed region the propagation losses are highlighted.

Two factors are used to characterize the performance devices: the total efficiency η and splitter efficiency η_{splitter}. The total efficiency represents the insertion losses, which is the ratio between the input and output power, ie $\eta = P_{\mathrm{out}}/P_{\mathrm{in}}$. The splitter efficiency quantifies only losses due to the curvature and the division of light from the device. Then, the efficiency of the splitter is:

$$\eta_{\mathrm{splitter}} = \frac{1-\eta_0}{1-\eta} \tag{6}$$

where η_0 and η are the total efficiency of the straight waveguide and power splitter, respectively, with the same total length. In this way, we can calculate losses by bending and splitting of light and compare the performance between the three devices, see table 1. There are important differences between the efficiencies in the η_{splitter} factor. For this reason, the device performance could easily be measured in experimental samples.

For the experiments, five samples of each circuit type were fabricated, including the straight waveguides. Then, the propagation modes of the electromagnetic field at the output were measured by capturing the intensity profile with a CCD camera. Figure 8 shows the modes corresponding to a (a) straight guide, (b) CCS splitter, (c) curved splitter and (d) straight splitter. With the experimental configurations used, and due to the effects of coupling instability, higher-order modes manifested. It should be noted that in a straight splitter the bending angle forces the mode TM_{01}, as seen in figure 8(d), however it is reduced in CCS splitter, figure 8(b).

A statistical analysis of data was carried out. Five different measurements of each written circuit were taken, coupling and decoupling the light input in each case with the same input power and same conditions. In this way it is possible to set a randomness in the measurements. In conclusion, 100 measurements were performed, ie 5 measurements of 5 samples of 4 device types. The mode's intensity profile

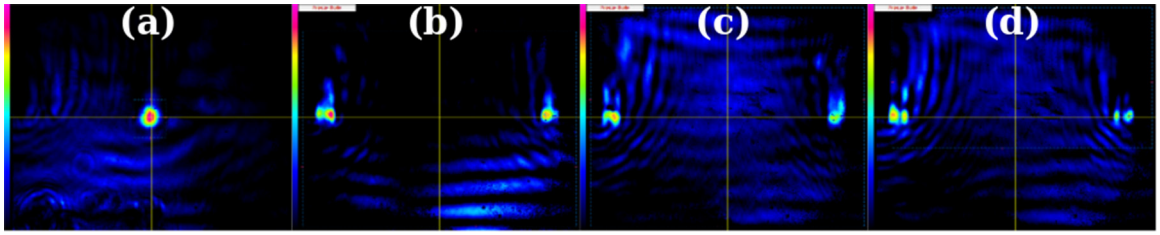

Figure 8. Propagation modes in the devices' output ($\lambda = 980$ nm to 20 mW). (a) Straight guide, (b) CCS splitter, (c) curved splitter, (d) straight splitter.

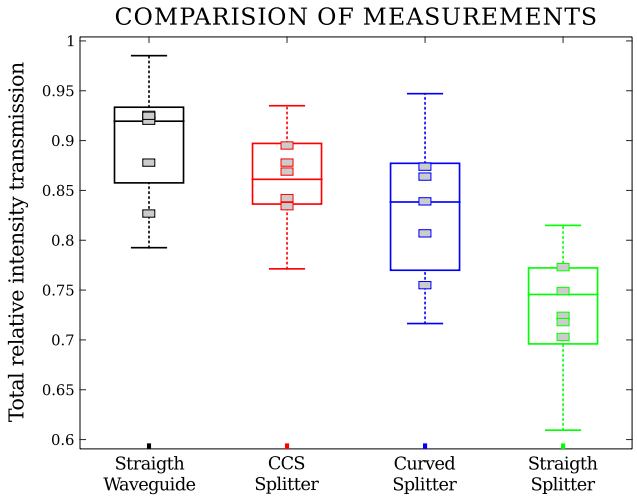

Figure 9. Box-plot [24] of all the relative power measurements by device type.

is integrated knowing that this is proportional to the output power. Figure 9 shows a box-plot [24] where 100 measurements are compared. In this graph, maximum and minimum values are represented by dotted lines. The bottom and top of the box are the first and third quartile respectively, and the band line inside is the median, and then the symmetry of the data is shown. Further, outliers may be plotted as a summation symbol. Also, the measurements averages are shown as scatter squares in figure 9 and table 1 shows the average efficiencies of the measurements. Finally, the insertion losses in the splitter are: 3.7 dB (CCS divider); 3.8 dB (curved divider); 4.4 dB (straight divider).

With all the experimental data, a Fisher test of multiple comparison hypotheses or LSD (Least Significant Difference) was conducted. The results show significant differences with a 5% error. This means that we can consider that the average represents values of different populations. Moreover, the CCS splitter is the device with the greatest efficiencies. Likewise, the measurements are similar to the values of the simulation results.

A box-plot of the coupling ratio between both branches of the splitter is shown in figure 10. This mainly helps us to visualize the median deviation and power distribution of the output (how much slide for each measurement to the left and right output), and for this reason the distribution of the box-plot is symmetric. A positive correlation between dispersion and losses is noted. The variations are 4.5%, 10.2% and 28.3%

Table 1. The simulation efficiencies and the average efficiencies of measurement are compared and shown by device type. The propagation losses of the simulations are estimated, see figure 7.

Sample	Straight Waveguide	CCS Splitter	Curved Splitter	Straight Splitter
Simulation results				
$\bar{\eta}$	0.895 (η_0)	0.872	0.830	0.742
$\bar{\eta}_{\text{splitter}}$	—	0.820	0.618	0.407
Experimental results				
$\bar{\eta}$	0.895 (η_0)	0.864	0.828	0.733
$\bar{\eta}_{\text{splitter}}$	—	0.770	0.610	0.394

for the CCS, curved and straight splitter, respectively. The percentage power distribution is significantly more balanced in the design based on coherent coupling.

Finally, some interesting behaviour that could be related to the uncertainties and limitations of the micromachining station are discussed. From table 1, we can see that the efficiencies calculated in the simulations are similar to the experimental results, so we think that the relative error of writing fluence does not have a relation to the insertion losses. In contrast, noticeable differences between the coupling balance and simulation results were observed among the fabricated devices (see figure 10). This fact can be attributed to spurious effects in the writing process, such as errors in the displacement or noise in the modification of the refractive index (mainly due to fluctuations in the writing energy). The straight splitter has the most unbalanced coupling ratio and insertion losses, hence, we think that the spurious effects are related to bending losses since the disturbances in the splitting zone might be converted in the radiation modes. The curved and CCS splitters behave differently. They have similar insertion losses, but the unbalanced coupling ratios notably differ amongst them, so the losses are not enough to explain it all. Figure 4 allows us to see that each device, depending on the interpolation distance (horizontal axis), corresponds to a different $\sigma/\bar{F}$ ratio, showing consequently different optical performance due to the writing fluence and kinematic uncertainty. In this way, the coupling balance can be considered a useful means to understand the role of the relationship between the relative error of the writing fluence and spurious effects on the direct writing process.

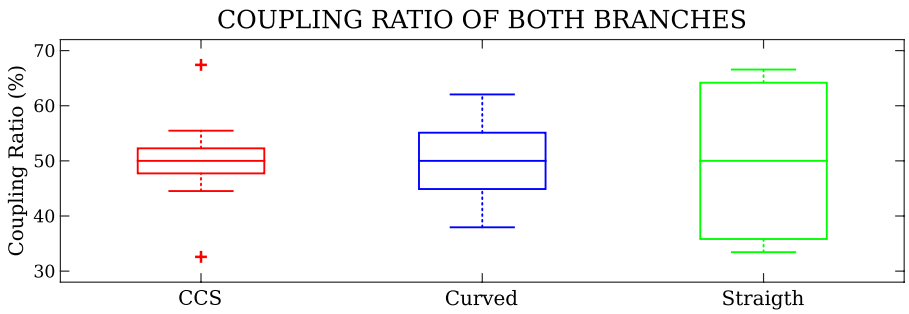

Figure 10. Box-plot [24] of the coupling ratio of both branches by splitter type.

5. Conclusions

In this work, we first present a 1 × 2 Y-branch power splitter in x-cut LiNbO3, based on simplified coherent coupling and built with direct femtosecond laser writing. The proposed design is compared with two other types of splitters, showing that the CCS circuit has lower losses. We verified the results with simulations and experiments. We used a solid statistical analysis of 100 measurements taken on 25 samples and obtained significant results for 5% of error; achieved 3.7 dB ± 0.1 dB losses in the CCS splitter and 4.5% coupling ratio variation. However, in detail, we explain the considerations used to design a systematic method that starts from the uncertainties and limitations of the motorized movement station to determine the trade-off to be taken into account in the design of a photonic circuit. For this, a new theoretical framework is developed that links kinematic and writing fluence of the process and allows us to establish which is the best geometry. Furthermore, it is shown for the first time that optimization of a CCS splitter depends not only on the length of the straight segments, but also on the bending angle, and even more, it is the first report that uses this geometry in waveguides with a non-step profile refractive index. In conclusion, a compact and low-loss 1 × 2 Y-branch power splitter is achieved with a simple and rapid fabrication technique, resulting in an analysis of the micromachining equipment specifications. In future work, we will link the relationship between the relative error writing fluence and the propagation losses, in order to determine how this significantly influences the device losses.

Acknowledgments

This work was partially supported by Universidad Nacional de Quilmes (Argentina) under project POP0771/16 and Agencia Nacional de Promoción Científica y Tecnológica (Argentina) under project 2016-4086. FV and VG are with CICBA (Argentina). GAT and RP are members of CONICET (Argentina).

ORCID iDs

G A Torchia https://orcid.org/0000-0002-6817-5312

References

[1] Lifante G 2003 *Integrated Photonics: Fundamentals* (New York: Wiley)
[2] Agrell E *et al* 2016 *Pure Appl. Opt.* **18** 063002
[3] Thompson M G, Politi A, Matthews J C and O'Brien J L 2011 *IET Circuits Device Syst.* **5** 94–102
[4] Lim A E J, Song J, Fang Q, Li C, Tu X, Duan N, Chen K K, Tern R P C and Liow T Y 2014 *IEEE J. Sel. Top. Quantum* **20** 405–16
[5] Righini G C and Chiappini A 2014 *Opt. Eng.* **53** 071819
[6] Davis K M, Miura K, Sugimoto N and Hirao K 1996 *Opt. Lett.* **21** 1729–31
[7] Tan D, Sharafudeen K N, Yue Y and Qiu J 2016 *Prog. Mater. Sci.* **76** 154–228
[8] Phillips K C, Gandhi H H, Mazur E and Sundaram S 2015 *Adv. Opt. Photonics* **7** 684–712
[9] Roberto Osellame G C and Ramponi R (ed) 2012 *Femtosecond Laser Micromachining* (Berlin: Springer)
[10] Jabłoński R, Turkowski M and Szewczyk R (ed) 2007 *Recent Advances in Mechatronics* (Berlin: Springer)
[11] Tan K K, Lee T H and Huang S 2008 *Precision Motion Control* (London: Springer)
[12] Mittholiya K, Anshad P K, Mallik A, Bharadwaj S, Bhatnagar A, Dharmadhikari J, Bernard R, Mathur D and Dharmadhikari A 2014 *12th Int. Conf. on Fiber Optics and Photonics* (OSA)
[13] Watanabe W, Matsuda K, Hirono S and Mochizuki H 2012 *J. Laser Micro Nanoeng.* **7** 171–5
[14] Wu Y, Wang C Y, Jia W, Ni X, Hu M and Chai L 2008 *Chin. Opt. Lett.* **6** 51–3
[15] Hsu C W, Chen H L and Wang W S 2003 *IEEE Photonics Technol. Lett.* **15** 1103–5
[16] Newport Corporation, Inc. 2015 SMC100CC and SMC100PP—Single-Axis Motion Controller/Driver for DC or Stepper Motor v3.0 https://newport.com/p/SMC100CC
[17] Synopsys, Inc. 2011 BeamPROP v8.3 -RSoft User Guide http://optics.synopsys.com/rsoft
[18] Neyra E, Suarez S and Torchia G 2014 *Opt. Lett.* **39** 1125–8
[19] Taylor H F 1974 *Appl. Opt.* **13** 642–7
[20] Johnson L and Leonberger F 1983 *Opt. Lett.* **8** 111–3
[21] Su J J and Wang W S 2002 *IEEE Photonics Technol. Lett.* **14** 1112–4
[22] Hutcheson L, White I A and Burke J J 1980 *Opt. Lett.* **5** 276–8
[23] Guarepi V, Perrone C, Aveni M, Videla F and Torchia G A 2015 *J. Micromech. Microeng.* **25** 125023
[24] McGill R, Tukey J W and Larsen W A 1978 *Am. Stat.* **32** 12–6